remote sensing

MDPI

Article

Using Advanced InSAR Techniques and Machine Learning in Google Earth Engine (GEE) to Monitor Regional Black Soil Erosion—A Case Study of Yanshou County, Heilongjiang Province, Northeastern China

Yanchen Gao [1,†], Jiahui Yang [1,†], Xiaoyu Chen [1], Xiangwei Wang [1], Jinbo Li [1], Nasrin Azad [1,2], Francis Zvomuya [3] and Hailong He [1,3,*]

[1] College of Natural Resources and Environment, Northwest A&F University, Xianyang 712100, China; gaoyanchen@nwafu.edu.cn (Y.G.); jiahui.yang@nwafu.edu.cn (J.Y.); chenxiaoyu@nwafu.edu.cn (X.C.); xw.wang@nwafu.edu.cn (X.W.); jinbo.li@nwafu.edu.cn (J.L.); n.azad@nwafu.edu.cn (N.A.)
[2] Department of Water Engineering, Faculty of Water and Soil Engineering, Gorgan University of Agricultural Sciences and Natural Resources, Gorgan 4913815739, Iran
[3] Department of Soil Science, University of Manitoba, Winnipeg, MB R3T 2N2, Canada; francis.zvomuya@umanitoba.ca
* Correspondence: hailong.he@hotmail.com
† These authors contributed equally to this work.

Abstract: The black soil region experiences complex erosion due to natural processes and intense human activities, leading to soil degradation and adverse ecological and agricultural impacts. However, the complexities involved in quantifying regional erosion poses remarkable challenges in accurately assessing the current status of regional soil erosion for effective soil conservation. To solve this issue, we proposed a new method for monitoring soil erosion using Interferometric synthetic aperture radar (InSAR) technology and machine learning algorithms within the Google Earth Engine platform. The new method not only enables regional-scale monitoring, but also ensures high accuracy in measurement (millimeter-level). The erosion susceptibility of the study area (Yanshou County, Heilongjiang Province, Northeastern China) was also classified using random forest algorithms to refine the monitored and predicted soil erosion. The results indicate that the five-year (2016–2021) deformation in Yanshou County was −11.08 mm, with a significant mean cumulative deformation of −8.08 mm yr^{-1} occurring in 2017. The driving factor analysis shows that the region was subject to the compound effect of water and freeze–thaw erosion, closely related to crop phenological stages. The susceptibility analysis indicates that 73.3% of the region was susceptible to erosion, with a higher probability in river areas, at high altitudes, and on steep slopes. However, good vegetation cover can reduce the risk of soil erosion to some extent. This study offers a new perspective on monitoring regional soil erosion in the black soil region of China. The proposed method holds potential for future expansion to monitor soil erosion in a larger areas, thereby guiding the strategies development for protection of the agriculturally important black soil.

Keywords: erosion susceptibility; SBAS-InSAR; D-InSAR; deformation velocity; soil and water conservation

Citation: Gao, Y.; Yang, J.; Chen, X.; Wang, X.; Li, J.; Azad, N.; Zvomuya, F.; He, H. Using Advanced InSAR Techniques and Machine Learning in Google Earth Engine (GEE) to Monitor Regional Black Soil Erosion—A Case Study of Yanshou County, Heilongjiang Province, Northeastern China. *Remote Sens.* **2024**, *16*, 3842. https://doi.org/10.3390/rs16203842

Academic Editor: Giuseppe Casula

Received: 10 September 2024
Revised: 10 October 2024
Accepted: 12 October 2024
Published: 16 October 2024

1. Introduction

Black soils or prairie soils are endowed with exceptional physical properties and nutrient contents, being ideal for plant/crop growth. They possess abundant fertility, superior water and nutrient retention capacities, optimal aeration, and a favorable soil structure that promotes extensive root growth and extension [1,2]. The primary black soil regions, which constitute approximately 916 million ha or 7% of the Earth's ice-free land area, are located in mid-latitudes of North America (e.g., United States, Canada and Mexico),

South America (e.g., Argentina and Uruguay), Eurasia (e.g., southern Russia and Ukraine) and northeastern China [3]. These regions are crucial food-producing areas within their respective countries and play an indispensable role in global food security [4–6]. However, black soils worldwide are currently under a severe threat of degradation. According to the Global Black Soil Report published by the Food and Agriculture Organization [7], most black soils have experienced a substantial depletion of around half of their organic carbon stocks, along with moderate to severe soil erosion. They also face the risks of nutrient imbalance, acidification, soil compaction, and loss of biodiversity [8]. More than four decades of overexploitation and unsustainable land use in the Black Soil Region (BSR) of northeastern China have further exacerbated soil erosion, leading to significant degradation of both soil quality and productivity.

Given the current critical situation, there is a need to assess the status of the black soils in a timely and accurate manner and to formulate effective protection measures. Therefore, the imperative to safeguard black soils necessitates rapid and precise monitoring of soil erosion across extensive areas. Research on black soil erosion is categorized into five spatial scales: sample points and slopes [9,10], sub-watersheds, watersheds, and regions. LiDAR (Light Detection And Ranging) and fixed-point monitoring techniques based on root exposure [11], which have been widely employed at the sample-point scale to monitor the local factors influencing erosion dynamics, such as microtopography, climate, and soil properties. Previous studies on the monitoring of slope erosion and sub-watershed erosion using methods such as isotope tracing or runoff plots aimed to investigate various factors, including soil erodibility, erosive sediment sources and gully erosion development processes [12]. For watershed and regional-scale studies, the main methods encompass the construction of process-based models, such as the Revised Universal Soil Loss Equation (RUSLE) [13–15], the Chinese Soil Loss Equation (CSLE) [16], the Soil and Water Assessment Tool (SWAT) [17,18], APEX [19,20], the Water and Tillage Erosion Model and Sediment Delivery Model (WATEM/SEDEM) [21,22], the Limburg Soil Erosion Model (LISEM) [23–25], and the Morgan–Morgan–Finney model (MMF) [26,27]. These are complemented by remote sensing monitoring and hydrological monitoring [28]. While a large number of studies on the erosion of black soils have been conducted so far, the primary focus has been on gully erosion [29,30], slope erosion, and small watershed erosion [31–33]. Studies focusing on large-scale regional erosion have mainly employed process models such as RUSLE or hydrological remote sensing monitoring [34,35]. Although these methods meet the needs of large-scale studies, they are affected by the resolution of images or related data, leading to low accuracy. Consequently, there is an urgent need to identify a regional-scale monitoring technique that can meet the requirement of large-scale monitoring while ensuring millimeter-level vertical accuracy [36,37].

Interferometric synthetic aperture radar (InSAR) is a technique for monitoring surface deformation [36,38] that has been widely used in research fields such as geological hazards [39–41], groundwater storage monitoring [42,43], construction monitoring [44,45], and mine deformation [46,47]. Several studies have utilized Small Baseline Subsets Interferometric Synthetic Aperture Radar (SBAS-InSAR) to effectively monitor landslide activity in northern California and southern Oregon, revealing a strong association between landslides and precipitation [48–50]. Time-series InSAR has been employed in multiple studies to investigate the long-term land subsidence patterns at Hong Kong Airport and Kochi airport [51] over the past two decades, establishing a significant correlation between subsidence and factors such as landfill materials, underlying alluvial sediments, and reclamation project stages [52]. Furthermore, time-series InSAR techniques have been successfully applied to monitor glacier displacements and tropical forest disturbances in northern Alaska, demonstrating their wide applicability with high accuracy [53,54]. These findings collectively highlight the extensive potential of InSAR technology for large-scale deformation monitoring, particularly in soil erosion assessment [55,56]. Satellite-borne InSAR offers the advantage of acquiring extensive regional data, thereby overcoming limitations associated with conventional monitoring methods such as subjective field distribution,

limited spatial resolution, and high costs. Additionally, since soil erosion involves soil relocation and deposition, it essentially represents a form of surface deformation. Hence, InSAR technology can be employed to effectively assess large-scale changes in the thickness of the surface soil layer at high spatiotemporal resolutions, providing valuable insights into regional soil erosion levels. Moreover, this approach eliminates the need for expensive long-term field monitoring stations, while ensuring continuous regional monitoring at 12-day intervals, thus making it highly advantageous for large-scale, continuous, regional soil erosion assessment.

Currently, the black soil region of northeastern China faces multiple forms of compound erosion, including water, wind, freeze–thaw, and gravity [57]. According to the Black Soil Conservation and Utilization Report [58], the black soil zone experienced a total of 221,600 km^2 of soil erosion in 2018. Mild erosion was found to be dominant, accounting for 73.8% of the affected area, with approximately 70% of this type of erosion being on arable land. The average annual erosion rate in the BSR is about 2.2 mm yr^{-1} [59]. This is further exacerbated by unsustainable human land-use practices that are accelerating the erosion of this valuable land [60]. These factors have had a significant impact on the ecological environment and agricultural production in the region [61,62]. In order to cope with this serious situation, accurate monitoring of soil erosion status on a regional scale and effective assessment of susceptibility are necessary. Susceptibility analyses and early warnings for regional erosion are urgently needed to reduce black soil erosion. Through the utilization of advanced radar remote sensing monitoring technology and Google Earth Engine (GEE), it is possible to achieve precise monitoring and prediction of soil erosion, providing a scientific basis for the formulation of targeted prevention and control measures. In addition, these monitoring and prediction results can also serve as valuable reference points for the modeling of regional soil erosion disasters. By conducting a comparative analysis on soil erosion at different time intervals, potential disaster risks can be identified in a timely manner, enabling the implementation of effective preventive measures and minimizing disastrous losses.

Yanshou County is situated in a typical black soil region of northeastern China, characterized by an intricate network of rivers and abundant water resources, rendering it a prominent hub for grain production. Simultaneously, this area exhibits diverse geomorphological structures and complex topography, particularly marked by numerous ditches along the periphery of low mountainous terrain, leading to severe soil erosion. This study focuses on Yanshou County as a representative sampling site in the BSR to conduct comprehensive monitoring and address regional soil erosion issues.

The objectives of this study were to (1) investigate and validate the deformation and velocity of soil erosion in the Yanshou County through a long-term time series analysis using InSAR technology, (2) analyze the dynamic alterations and primary driving factors influencing soil erosion in the Yanshou County, and (3) integrate the existing RUSLE model's relevant datasets, soil data, and cultivation information on the GEE platform to accurately and comprehensively assess the susceptibility to soil erosion.

2. Materials and Methods

2.1. Study Area

This study was conducted in Yanshou County (3149 km^2) in the southeastern part of Heilongjiang Province, Northeast of China. Yanshou County has a cold-temperate continental monsoon climate, characterized by cold and dry conditions and a long freezing period in winter, and concentrated precipitation in the warm, humid summer. This region has an average annual temperature of 2.3 °C and an average annual precipitation of 571.7 mm. The general terrain slopes from the south and north toward the middle, and the middle slopes from the southwest toward the northeast, with the lowest elevation point 110 m above mean sea level. The area is characterized by four types of terrain: low mountains, hills, terraces, and plains. The low mountain and hilly areas are affected by erosion and are mostly composed of granite and some Paleozoic metamorphic rock series.

There are many ditches and forks on the edge of low mountainous areas, with complex terrain and severe soil erosion. The plateau and plain areas are distributed on both sides of the Maqian River valley and are affected by erosion from rivers such as the Maqian River. The area is rich in water sources, flat terrain, and fertile land, making it the main grain-producing area in Yanshou County (Figure 1).

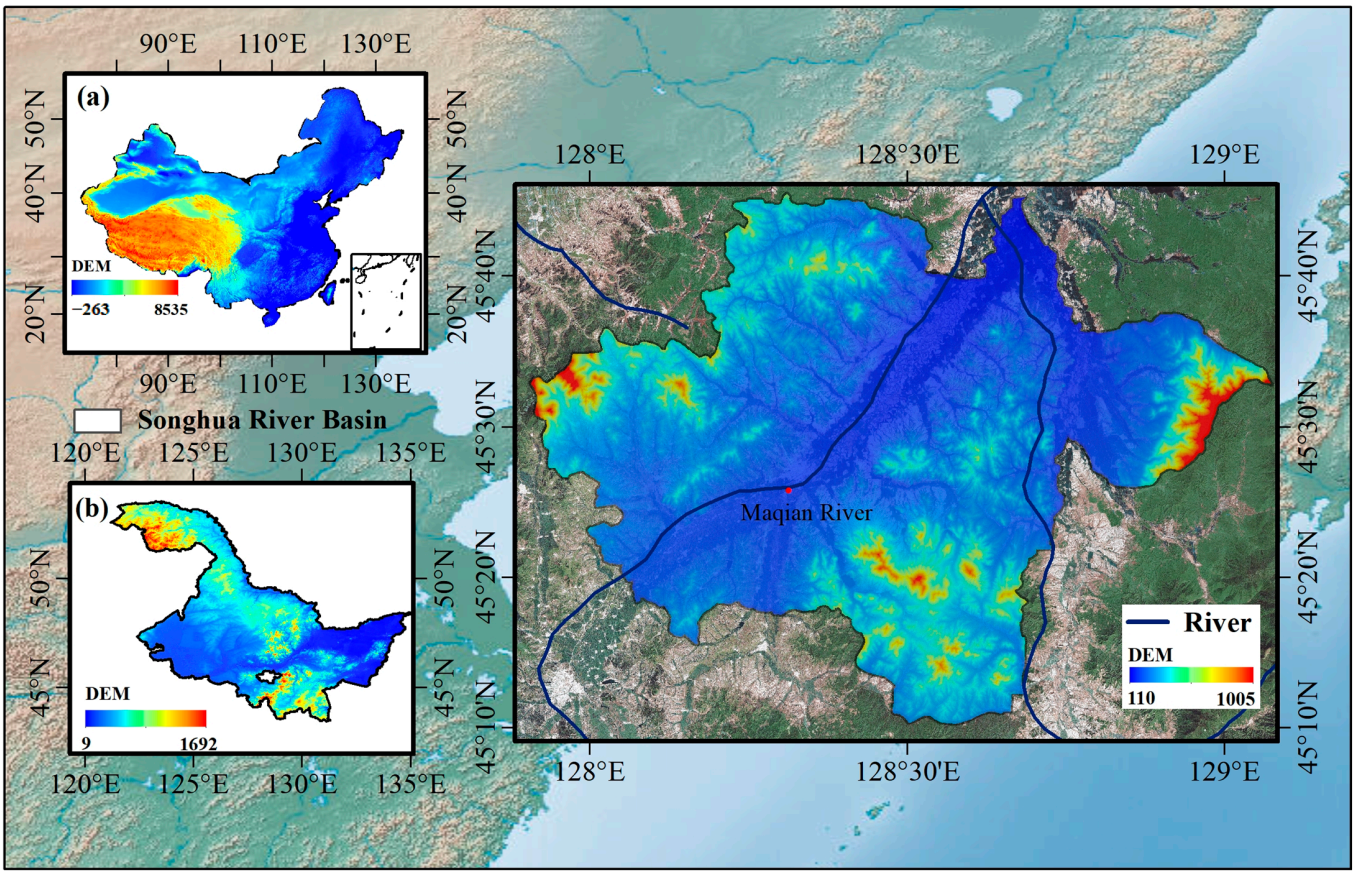

Figure 1. Geographic location of Yanshou County, Heilogjiang Province, China, (**a**) in the northeast black soil region and (**b**) in Heilongjiang Province.

2.2. Data

2.2.1. InSAR Data

Sentinel-1 consists of two polar-orbiting satellites. Its C-band synthetic aperture radar imager can obtain images without being affected by clouds and water vapor. The data obtained by radar has certain penetration, which can reduce the influence of high-density vegetation on monitoring [63]. The D-InSAR analysis images were divided into two pairs, which were acquired from 2 October 2016 to 11 December 2021 and from 6 January 2017 to 20 December 2017, respectively. The SBAS-InSAR analysis obtained 25 Sentinel-1 C-band IW VV SLC images with a spatial resolution of ~15 m through the descending orbit from 6 January 2017 to 20 December 2017. The specific parameters of Sentinel-1 image data and the temporal and spatial baseline connection graph of the time series interferogram pairs are presented in Table 1 and Figure S5, respectively.

Table 1. Basic parameters of synthetic aperture radar (SAR) image data and their specific data acquisition time.

SAR Data Parameter	Sentinel-1 B
Satellite (path)	Descending
Polarization	VV
Beam mode	IW
Wave band	C
Orbit	Path 32
Pixel spacing (Rg × Az) (m)	2.3 × 14.1
Wave length	5.6 cm
Time interval for image acquisition/(days)	~12
Image time range (D-InSAR)	2016–2021 (multi-year)/2017 (single)
Image time range (SBAS)	6 January 2017 to 20 December 2017
Quantity of images	25
SBAS-InSAR data Specific time	6 January, 18 January, 30 January, 11 February, 7 March, 19 March, 31March, 12April, 24 April, 6 May, 18 May, 30 May, 11 June, 23 June, 5 July, 29 July, 10 August, 22 August, 3 September, 15 September, 9 October, 14 November, 8 December, 20 December

2.2.2. Other Datasets

(1) Generic Atmospheric Correction Online Service (GACOS) for InSAR data: GACOS makes comprehensive use of high-resolution ECMWF data, GNSS tropospheric delay data, and high-precision DEM data to achieve the separation and estimation of water vapor components related to the terrain and those not related to the terrain, thus effectively improving the accuracy of atmospheric correction [64]. GACOS is globally applicable and has been widely used in the atmospheric and terrain correction of InSAR, significantly improving the accuracy of the InSAR results [65]. The time period related to GACOS data corresponds to the time node of InSAR data one by one, which provides a strong support for obtaining accurate geophysical information in time.

(2) Data sources for susceptibility analyses

The data selected for calculating the 15 characteristics of the susceptibility analyses are listed in Table 2, along with the data sets used for the acquisition of climatic characteristics, the calculation of the RUSLE model, and the single-band calculation. The resolution varied from 10 m to 5566 m, and the resolution of the data was unified to 1000 m by raster resampling through the GEE cloud platform, which was used for the erosion susceptibility analysis.

Table 2. The main datasets used in this study and their sources.

Datasets	Bands	Spatial Resolution (m)	Reference
CHIRPS Pentad: Climate Hazards Group InfraRed Precipitation with Station Data (Version 2.0 Final)	precipitation	5566	https://doi.org/10.1038/sdata.2015.66, accessed on 5 September 2024
NASA SRTM Digital Elevation 30 m	elevation	30	https://doi.org/10.1029/2005RG000183, accessed on 5 September 2024
OpenLandMap Soil Bulk Density	b0 (soil bulk density at 0 cm depth)	250	https://doi.org/10.5281/zenodo.1475970, accessed on 5 September 2024
OpenLandMap Sand Content	b0 (sand content at 0 cm depth)	250	https://doi.org/10.5281/zenodo.1476851, accessed on 5 September 2024
OpenLandMap Clay Content	b0 (clay content at 0 cm depth)	250	https://doi.org/10.5281/zenodo.1476854, accessed on 5 September 2024

Table 2. *Cont.*

Datasets	Bands	Spatial Resolution (m)	Reference
OpenLandMap Soil Water Content at 33 kPa (Field Capacity)	b0 (soil water content at 33 kPa (field capacity) at 0 cm depth)	250	https://doi.org/10.5281/zenodo.2629589, accessed on 5 September 2024
MCD12Q1.006 MODIS Land Cover Type Yearly Global 500 m	LC_Type1	500	https://doi.org/10.5067/MODIS/MCD12Q1.006, accessed on 5 September 2024
Sentinel-2 MSI: Multi-Spectral Instrument, Level-1C	B8, B4	10	Copernicus Sentinel Data Terms and Conditions.
OpenLandMap Soil Texture Class (USDA System)	b0 (Soil texture class (USDA system) at 0 cm depth)	250	https://doi.org/10.5281/zenodo.1475451 accessed on 5 September 2024
MYD13Q1.006 Aqua Vegetation Indices 16-day Global 250 m	EVI (Enhanced Vegetation Index)	250	https://doi.org/10.5067/MODIS/MYD13Q1.006, accessed on 5 September 2024

2.3. Study Framework and Methods

InSAR technology was applied to monitor the changes and deformation rates of soil layer thickness in BSR, with the change rate of regional soil layer thickness used as the training sample. The GEE platform was used to classify the susceptibility to regional erosion using machine learning (Random Forest) algorithm (Figure S2).

2.3.1. Acquisition of Long-Term Surface Deformation and Velocity with Interferometry Synthetic Aperture Radar (InSAR) Technique

Acquisition of Surface Deformation Change with D-InSAR

D-InSAR is a common technique used to obtain surface deformation information in an area by using SAR images of different phases through differential interferometry [66]. The Sentinel images from 2016 and 2021 were used to detect the changes in surface deformation over long time series using ENVI Sarscape 5.6.2 software in which the monitoring process was divided into several steps (Figure S3): (1) data pre-processing (Sentinel-1 C-band raw images were used to obtain Sentinel-1 SLC images of the target area through cropping and geo-pairing); (2) applying the two-orbit method using SAR images and DEM data for interferometric processing to obtain the corresponding intensity data; and (3) filtering the intensity data using a self-suitable filter, de-entangling, and performing orbit refinement to obtain the surface deformation results (Equation (1)):

$$\Delta R = \frac{\lambda}{4\pi}\left(\phi_{top+dem} - \phi_{top,sim}\right) \quad (1)$$

where ΔR denotes the ground deformation values (m), $\phi_{top+dem}$ denotes the interferometric results of the terrain phase, where the mathematical simulation process involves DEM data acquisition, and $\phi_{top,sim}$ denotes the interferometric results of the terrain and deformation phases, whose simulation process is acquired by the two views used for D-InSAR interferometric images.

Acquisition of Deformation Velocity with SBAS-InSAR

SBAS-InSAR is a differential interferometric technique based on multiple SAR images for generating surface deformation maps and the corresponding deformation rate changes. It can effectively overcome the incoherence of time and space by selecting multiple main images using appropriate spatiotemporal baseline thresholds to continuously monitor surface deformation in time series [67]. In this study, we selected 25 images for the whole year, from 6 January 2017 to 20 December 2017, for time-series InSAR monitoring to explore the reasons for the different trends of multi-year deformation and single-year deformation, via InSAR monitoring. This method entails a series of sequential steps encompassing data acquisition, interference, interference post-processing, deformation estimation, and the final deformation solution (Figure S4) [48]. The deformation monitoring results can be affected by noise, so in order to improve the accuracy of monitoring, the PSI points above a

coherence value threshold limit of <0.40 (which were non-ideal for deformation monitoring) were filtered [51].

2.3.2. Erosion Susceptibility Analysis with Machine Learning in Google Earth Engine (GEE)

This study aimed to use the machine learning classification algorithm to solve the problem of regional soil erosion susceptibility assessment in Yanshou County. The workflow diagram is given in Figure 2. Susceptibility was divided into the following steps: (1) Preprocessing: the RUSLE model and Double Logistic algorithms [68] were used to extract feature variables. This process yielded features such as the rainfall erosivity factor (R), the topographic factor (LS), the end of a growth season (EOS, Figure S1), etc. (Table 3). Specific algorithms are listed in the Supplementary Material. (2) Feature construction: the divided variables were categorized into three groups, including RUSLE erosion impact factors, natural factors, and cultivation (climatic). All selected feature bands were then fused to construct feature data collections using the GEE cloud platform. (3) Training sample generation: in the generation of training samples, a random sampling method was implemented to select 5000 deformation rate points from the 106,635 deformation points generated by the InSAR technique (Figure S6). Interpretive markers were generated based on the distribution of specific values of deformation points. The erosion susceptibility was classified into 16 categories, including 8 increasing (thickening) and 8 decreasing (erosion) categories. (4) Susceptibility classification: the random forest model was implemented to complete the delineation of erosion susceptibility. The number of random trees was set to 50, a decision based on an assessment of the data volume and the stability of the classification within the GEE cloud platform.

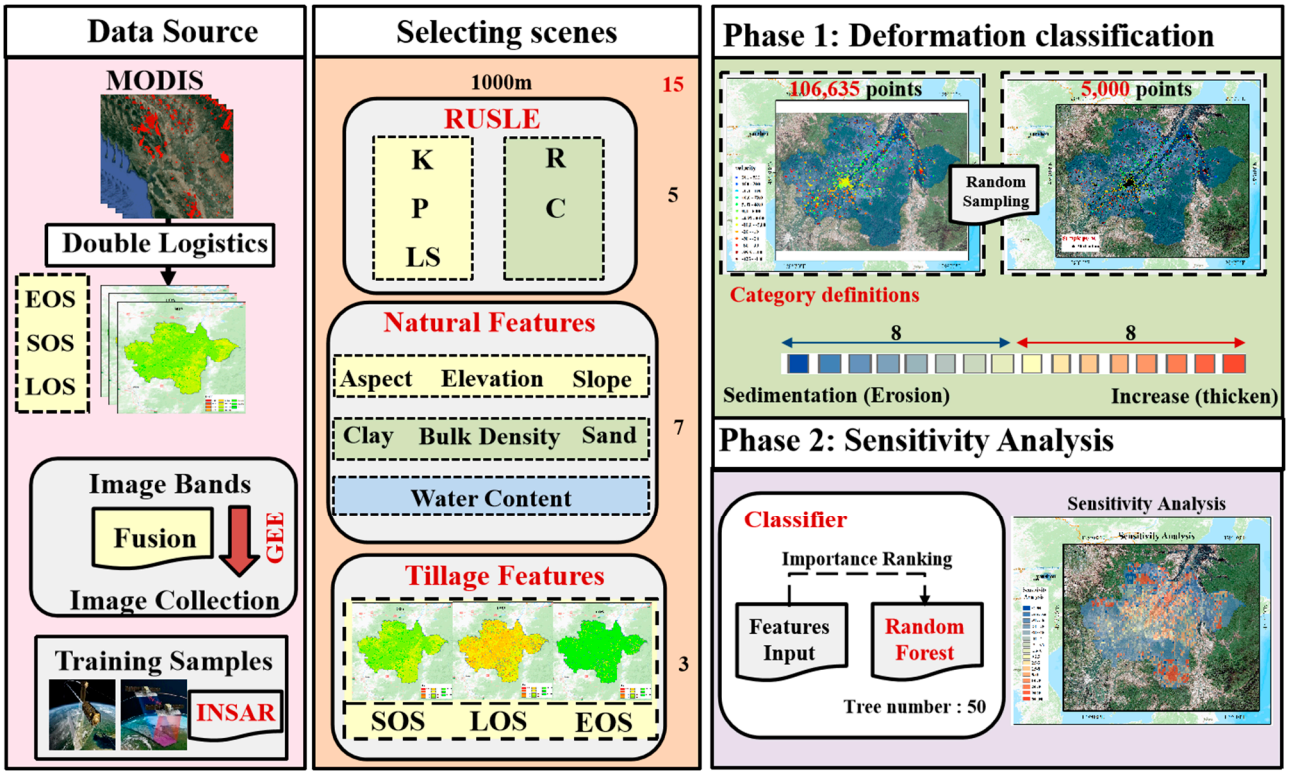

Figure 2. Construction of regional erosion susceptibility flowcharts using machine learning algorithms.

Table 3. Main sources of characteristic band used in susceptibility analysis and their corresponding calculation method.

Modules	Feature	Description	Calculation Method
RUSLE Figure 3	R	Precipitation erosion	[69]
	K	Soil erosion	[70]
	LS	Topographic	[71]
	C	Vegetation cover and management	[72]
	P	Soil and water conservation measures	[73]
Double Logistic Growth	SOS	Start of growth season (day)	[74–76]
	LOS	Lasting of growth season (days)	
	EOS	End of growth season (day)	

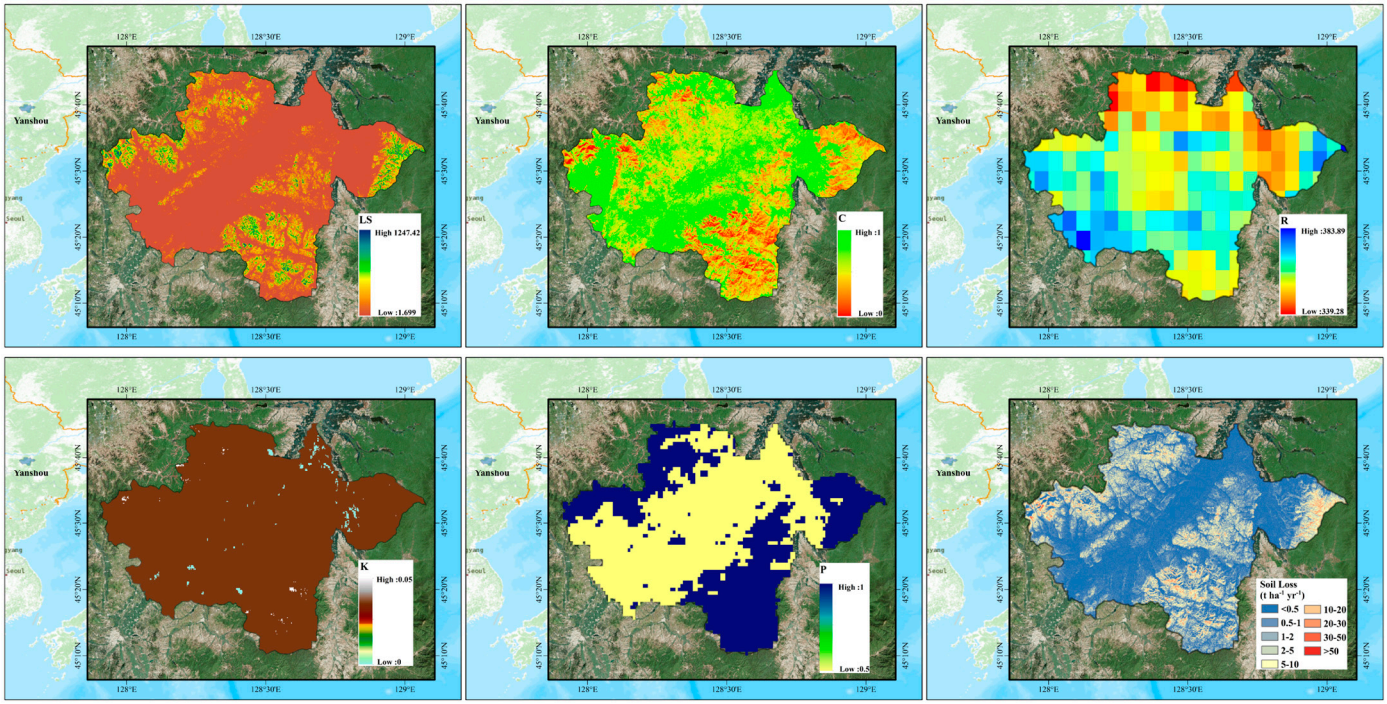

Figure 3. RUSLE (P R C K LS) multifactor spatial distribution. Soil loss represents the change in erosion simulated by the RUSLE model, P represents the soil and water conservation measures, R represents precipitation erosion, C represents vegetation cover and management, K represents soil erosion, and LS is the topographic factor.

2.3.3. Software and Google Earth Engine Cloud Platform

In this study, we opted to utilize SARscape 5.6.2 software for processing the D-INSAR and SBAS-INSAR procedures, simultaneously employing the Generic Atmospheric Correction Online Service (GACOS) data for atmospheric correction and interference result filtering [77]. The Google Earth Engine (GEE) cloud platform serves as a remote sensing big data platform that integrates data storage, online access, analysis, and processing [78]. In recent years, it has found extensive application in diverse research domains, such as forest degradation and climate monitoring [79], along with disaster early warning systems [80]. Moreover, the GEE cloud platform incorporates numerous machine learning algorithms; among them, random forest is widely favored due to its efficiency, speed, and robustness against overfitting issues [81,82]. In this study, we propose a comprehensive solution to address erosion susceptibility by leveraging the GEE cloud platform along with its embedded random forest algorithm.

3. Results

3.1. Calculation of Multi-Year and Single-Year Shape Variables in Yanshou County Using D-InSAR

The statistics indicate that the regional cumulative deformation ranged from −149.3 to 140.6 mm between 2016 and 2021, with a mean value of −11.09 mm in regional deformation, demonstrating a clear subsidence trend (Figure 4a). Based on the spatial distribution of residential areas, agricultural areas, and associated land use, it can be inferred that there might exist a reduction in the thickness of the soil layer in the region. The cumulative deformation distribution ranged from −171.8 to 152.9 mm in 2017, with a mean value of 5.6 mm (Figure 4b). The result contradicts the multi-year cumulative deformation, indicating an accumulation trend in the region, along with the thickening of the soil layer. Spatial analysis of the long-term regional deformation time series revealed that the built-up and planted areas exhibited minor settling ranging from 0.2 mm to 5 mm, whereas more pronounced settling (~20 mm) was observed along river banks in the central region. Some mountainous regions displayed noticeable accretion; however, within these areas, soil relocation resulted in subsidence on slopes and accretion in the adjacent lower areas. The single-year deformation analysis further indicated soil stacking in the eastern mountains and rivers, while slight subsidence (~10 mm) was observed in northeastern and southern hilly areas with more significant local erosion (>34 mm). Despite a similar overall trend to multi-year subsidence, distinct differences were apparent in local riverbanks and higher elevation regions.

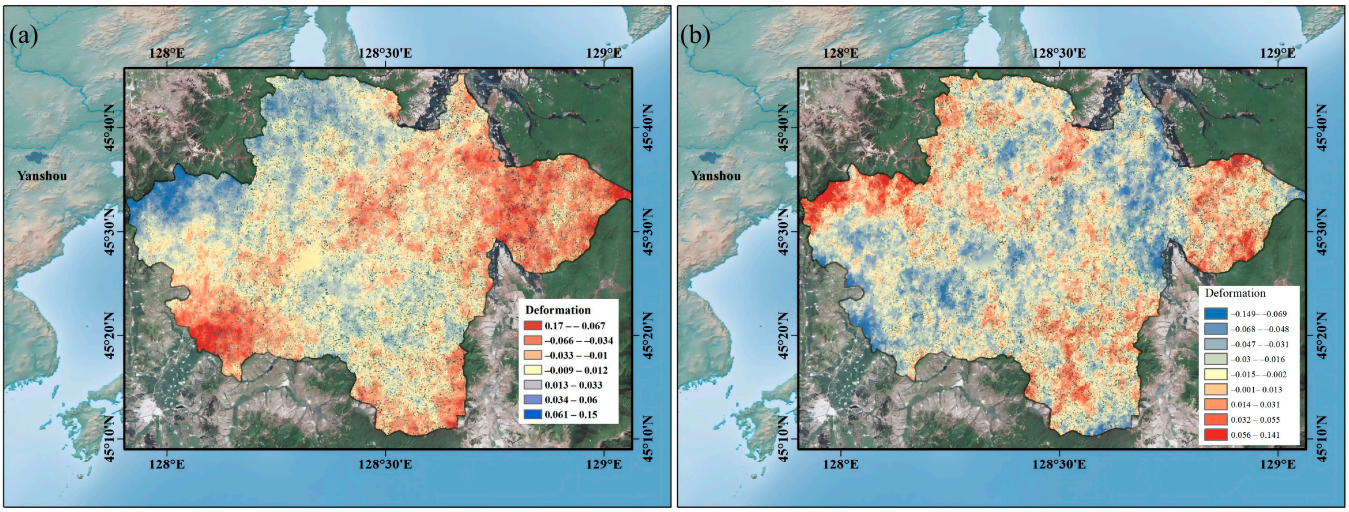

Figure 4. Long-term time series surface deformation results obtained by D-InSAR for Yanshou County: (**a**) average annual deformation from 2016 to 2021; (**b**) average deformation in 2017.

3.2. Calculation of Cumulative Deformation Rate Changes in Yanshou County Using SBAS-InSAR

Based on the 106,635 sample points gathered from SBAS-InSAR monitoring, the annual cumulative deformation rate was between −424.63 mm yr^{-1} and 521.96 mm yr^{-1}, with a spatial mean value of −8.08 mm yr^{-1} (RMSE: 3.442 mm). The distribution of cumulative velocity exhibited a higher degree of concentration, with 96,689 out of 106,635 significant deformation rate points falling within the velocity range of −50 to 30 mm yr^{-1}, accounting for a substantial proportion (90.7%) of the total (Figure 5). The distribution of the significant points was widest in the range from −10 mm yr^{-1} to 5 mm yr^{-1} (Figure 5B). Based on the spatial distribution information depicted in Figure 5A, it was evident that the central urban area and the river banks exhibited a higher density of significant points, indicating changes in deformation velocity. Conversely, the southern hilly area and northeastern hilly area displayed a lower number of such significant points; however, extreme points (deformation rate > 100 mm yr^{-1} or <−100 mm yr^{-1}) were more widely distributed. The deformation

rate distribution near the center of the city and the plantation area was more stable, with rates concentrated in the range of −10 to 5 mm yr^{-1}, and the overall tendency was for a slight subsidence.

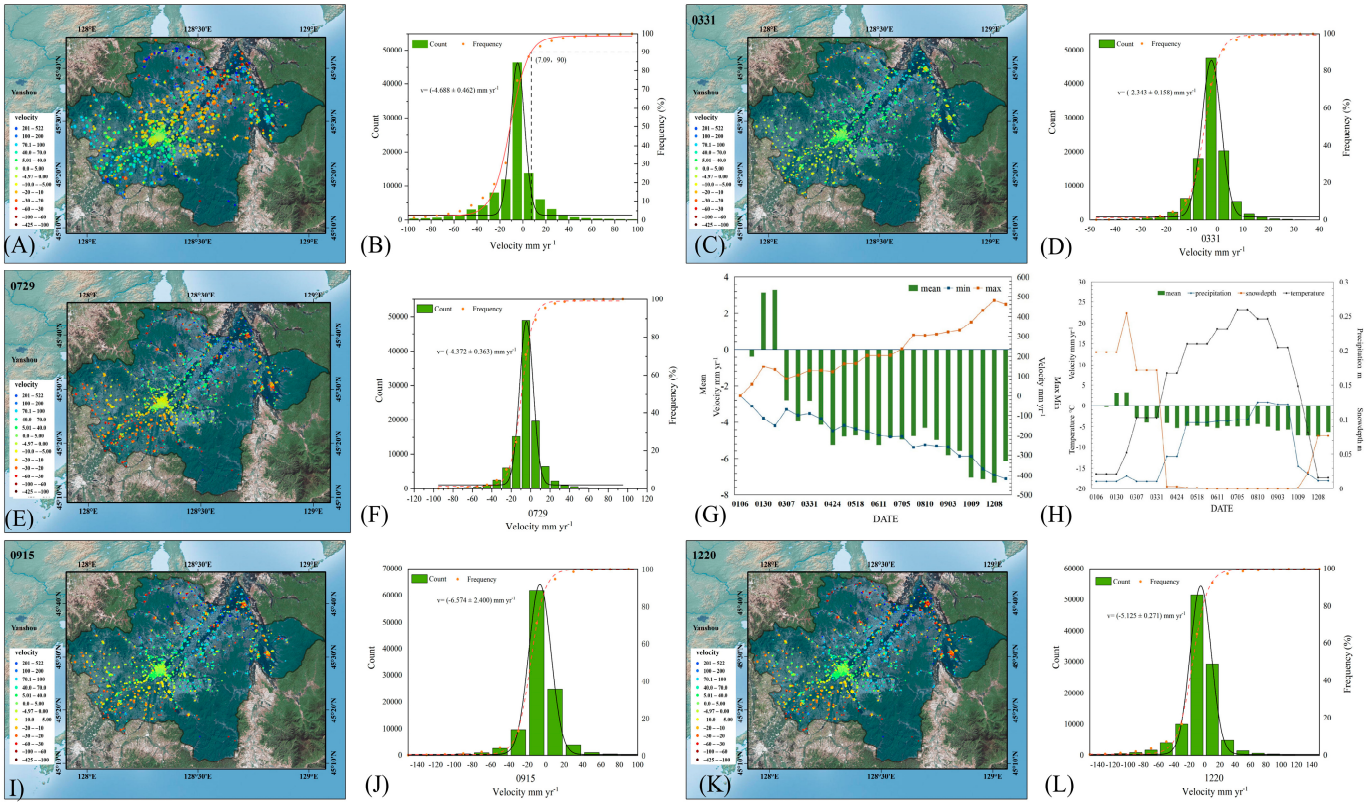

Figure 5. Distribution of the mean cumulative deformation rate in 2017, obtained using SBAS-InSAR monitoring: (**A**) spatial distribution of the mean cumulative deformation rate; (**B**) statistical distribution of the mean cumulative deformation rate. (**C**–**L**) Changes in cumulative deformation rate (mm yr^{-1}) in Yanshou County by season and node; (**C**,**E**,**I**,**K**) represent the spatial distribution of cumulative deformation rate on 31 March, 29 July, 15 September, and 20 December 2017, respectively; (**D**,**F**,**J**,**L**) represent the statistical distribution of cumulative deformation rate on 31 March, 29 July, 15 September, and 20 December 2017, respectively; (**G**) cumulative deformation rate versus temperature and precipitation; and (**H**) temporal variation of cumulative deformation rate with temperature, precipitation, and snow thickness.

In order to further reveal the changes in each season in Yanshou County, the annual-scale cumulative deformation rate was divided according to the time nodes of 31 March, 29 July, 15 September, and 20 December, 2017 and analyzed and processed in each of these time nodes. The mean cumulative deformation rate was −2.838 mm yr^{-1} on 31 March, −4.752 mm yr^{-1} on 29 July, −5.603 mm yr^{-1} in mid-September, and −6.142 mm yr^{-1} on 20 December (Figure 5), which was the lowest cumulative deformation rate across the four time nodes. The minimum mean cumulative deformation rate (−7.38 mm yr^{-1}) occurred on 8 December.

3.3. Statistical Analysis of Deformation Rate in Residential and Planting Regions

After the filtering and selection of SBAS-InSAR monitoring results with the criteria of coherence > 0.4, 31,151 monitoring sites were retained. From the spatial distribution analysis of the monitoring sites (Figure 6), the sites were mainly distributed in residential areas and agricultural cultivated land near rivers. The statistical analysis showed that the deformation rate of residential areas and agricultural cultivated areas was relatively gentle, with an annual mean value of −5.054 mm yr^{-1} (RMSE: 1.335 mm) and a standard deviation of 2.867 mm yr^{-1}, and the deformation velocity was mainly scattered in the range of −20 to 10 mm $yr-^{1}$ (Figure 6c). The time series results revealed that the soil layer thickness of residential areas and agricultural land had a gradually thinning trend, whereas the soil layer subsidence rate in other months was ~ −5 mm yr^{-1} to −4 mm yr^{-1}, except in March (Table 4). Residential areas and agricultural cultivated land began to experience the rainy season in April, and the settlement rate increased significantly, reaching a peak value at the end of the rainy season in September (Figure 7).

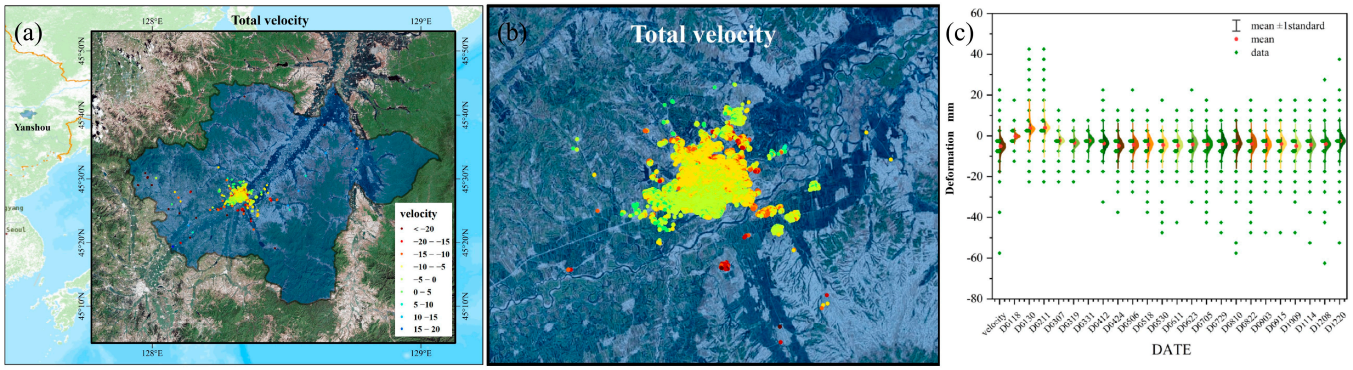

Figure 6. Changes in cumulative deformation rate (mm yr^{-1}) in residential and cultivated regions (coherence > 0.4): (**a**,**b**) spatial distribution of the mean cumulative deformation rate, (**c**) statistical distribution of the mean cumulative deformation in residential and planting regions.

Table 4. Descriptive statistics of cumulative deformation in residential and planting regions (unit: mm).

Deformation (mm)	Date												
	18 January	11 February	31 March	24 April	30 May	23 June	29 July	22 August	15 September	9 October	14 November	20 December	Velocity mm yr^{-1}
Max	18.1	41.6	9.8	12.4	19.7	21.4	14.4	17.5	15.4	16.6	19.8	35.9	21.909
Min	−12.2	−22.9	−17.9	−36.2	−45.3	−31.3	−45.1	−45.9	−47.2	−48.5	−51.7	−52	−57.173
Mean	−0.156	3.959	−2.339	−4.864	−4.513	−4.202	−4.043	−3.848	−3.886	−4.916	−4.375	−2.433	−5.054
Standard deviation	1.04	3.468	2.142	2.913	2.754	3.089	3.124	3.171	2.981	2.905	2.869	2.886	2.867

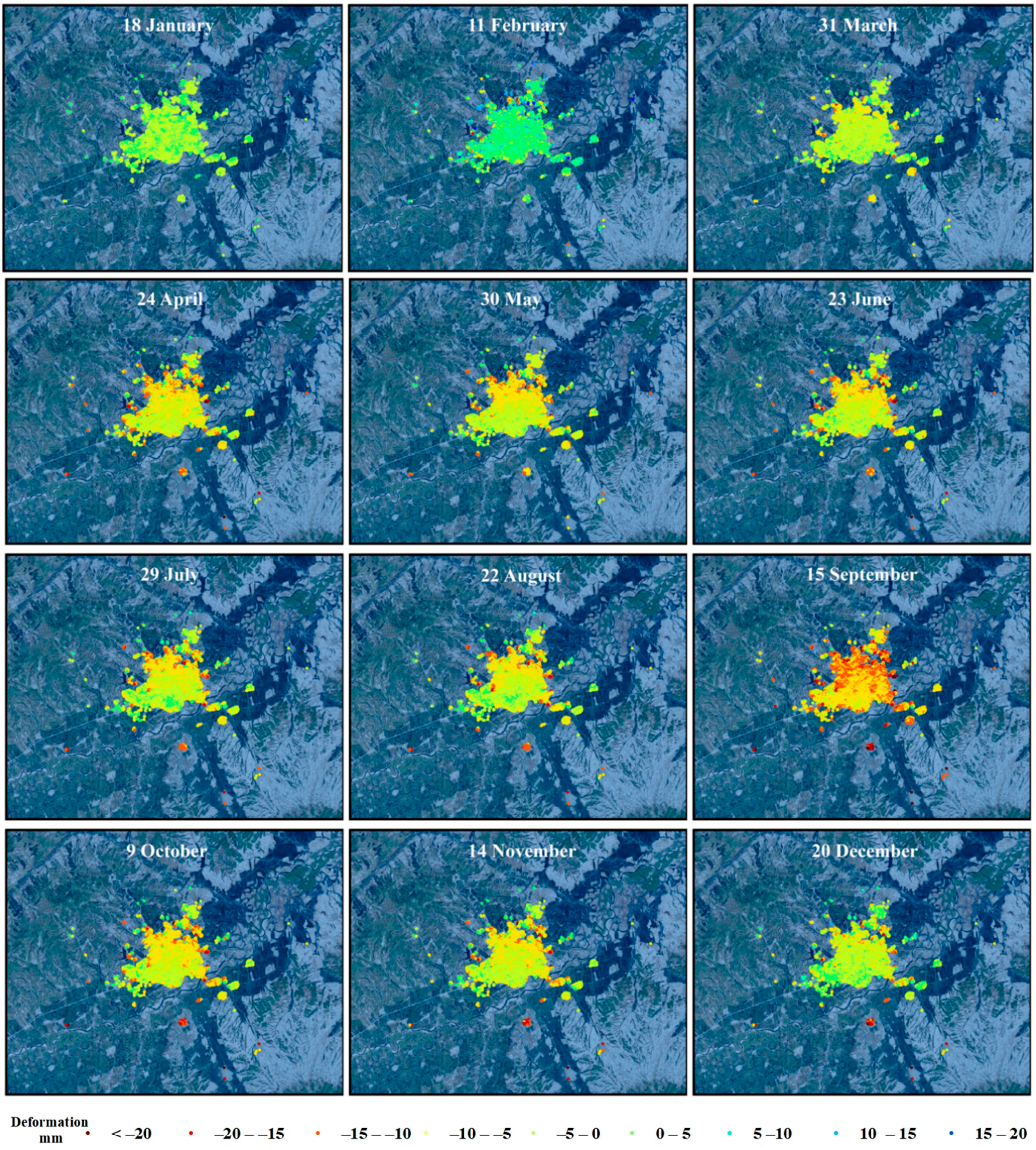

Figure 7. Monthly changes in cumulative deformation (mm) of residential and planting regions in Yanshou County during 2017.

3.4. Analysis of the Drivers of Deformation in Yanshou County

In order to further elucidate the drivers of regional deformation and the correlation between deformation and erosion, the four correlation factors of the RUSLE model, surface temperature, plant phenology information, and LOS, which all represent agronomic activities, were correlated with cumulative deformation rates in regions exhibiting significant

deformation. There was a moderate negative correlation between the changes in cumulative deformation rate and the precipitation erosion factor R (Figure 8a). As the erosion factor increased, the rate of subsidence in the region increased. The changes in deformation rate exhibited a weak correlation with surface temperature. An increase in ground temperature led to a tendency for the sedimentation rates to increase, but at a slower pace. Due to the complexity of land use types in the region and the mix of various factors, we employed the random forest method to assess feature importance rankings for potential factors affecting regional deformation. The feature importance ranking diagram (Figure 8b) revealed that cultivation had the most significant effect on regional deformation, followed by topographic factors (slope and aspect) and precipitation. Compared with cultivation and topography, the basic properties of soil had relatively little effect on regional deformation. Among the soil characteristics, bulk density, sand content, and soil moisture content were relatively more important.

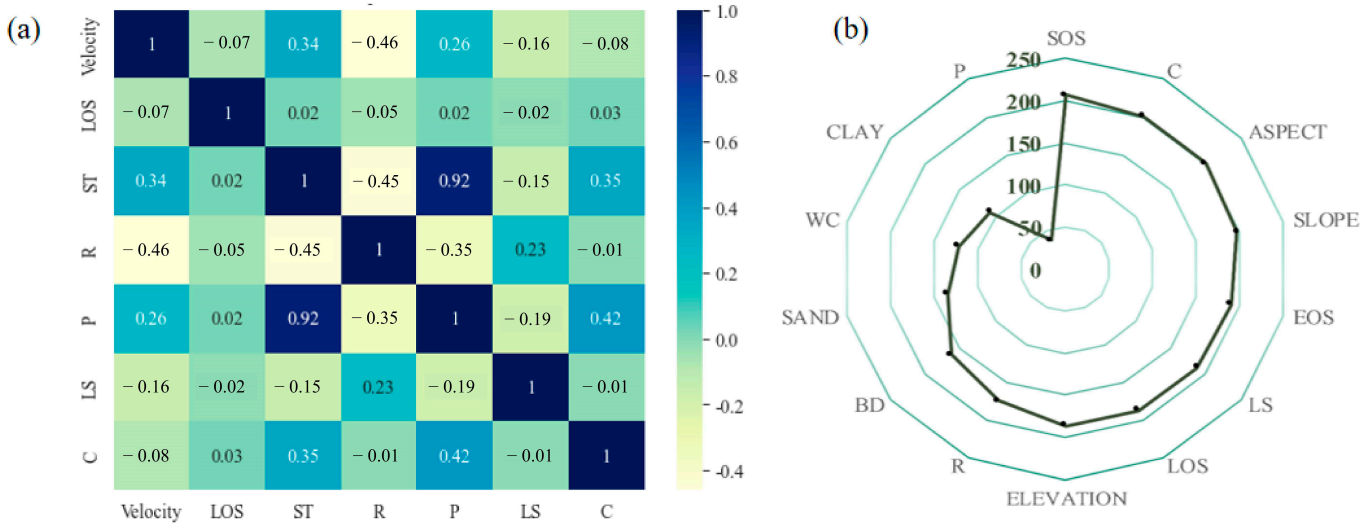

Figure 8. Correlation between cumulative deformation velocity and erosion-related factors. (**a**) Heat map of correlation between cumulative deformation rate and RUSLE factors. LOS: length of the season, ST: surface temperature. (**b**) Importance ranking of features affecting the change in deformation rate using the random forest algorithm. WC: water content, BD: bulk density.

3.5. Erosion Susceptibility Analysis for Yanshou County

The deformation in Yanshou County does not fully represent the current erosion status of the region, but the deformation rate of the surface in the BSR can indicate regional erosion and subsidence trends, as well as areas with severe deformation. To monitor soil erosion susceptibility in the BSR using regional deformation changes, we utilized actual deformation rates as training samples and selected relevant factors influencing black soil erosion as features for classifying regional susceptibility. Because a single deformation rate cannot reflect the erosion status of the whole region, the deformation rates distributed in the BSR were classified into eight classes of erosion and eight classes of accumulation for a total of 16 classes, according to the pattern of their distribution, and the regional erosion susceptibility was classified with the aid of the machine learning (random forest) algorithm. The distribution of erosion susceptibility gradually decreased from high altitude to low altitude (Figure 9a), while the erosion areas were adjacent to the depositional areas (blue areas are adjacent to red areas in the figure), which may be susceptible to scouring or gully erosion. At the same time, the residential areas and cultivated areas were prone to slight erosion, and some forested areas showed obvious sedimentation. The erosion susceptibility analysis revealed a significant risk of erosion activity in Yanshou County's BSR, accounting for approximately 73.3% of its total land cover. A proportion of 24.1% of the area (mountainous or hilly terrain, relatively high altitude) was prone to moderate erosion

(sedimentation rate between −50 mm yr^{-1} and −30 mm yr^{-1}), necessitating effective protection measures during precipitation events (Figure 9b).

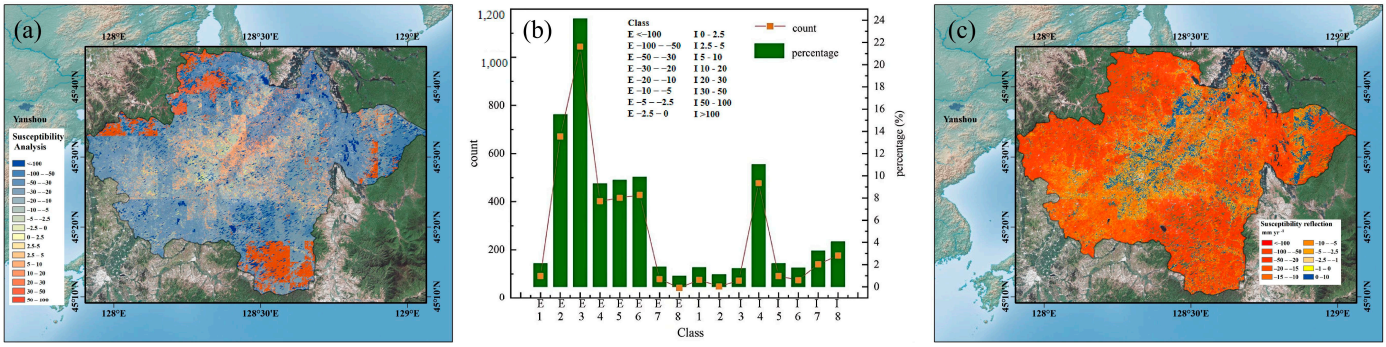

Figure 9. Spatial and statistical distribution of erosion susceptibility: (**a**) spatial distribution pattern of erosion susceptibility obtained using the random forest algorithm; (**b**) statistical distribution map of erosion area delineation; (**c**) cumulative deformation rate inversion results.

4. Discussion

4.1. Multi-Year and Single-Year Deformation Attribution Analysis in Yanshou County

The deformation monitoring results showed that the spatial mean values of single-year (2017) and multi-year (2016–2021) cumulative deformation in Yanshou County were 5.6 mm and −11.1 mm, respectively. There was a clear difference in the values and the direction of these two, with the overall deformation of the five-year period showing a tendency for the region to subside, whereas the single-year deformation showed a tendency to uplift. Previous studies showed that changes in groundwater resources may cause either subsidence or uplift in their study region, which was mainly related to the local geological and hydrological conditions [83]. According to a news report [84], July–August 2017 experienced heavy rainfall in many areas of Heilongjiang Province. This led to a substantial increase in the water levels of some rivers by up to 2 m, and heavy rainfall in a short period of time will cause the groundwater level to rise sharply [85]. Yanshou County is rich in hydrological resources and has many rivers. Among them, the Maqian River has a total length of 96.7 km in Yanshou, with a watershed area of up to 2818.8 km^2. The 2017 single-year deformation results showed more obvious sedimentation in the hilly area, while the mainstem of the Maqian River showed more pronounced subsidence (Figure 4b). Based on climatic elements and DEM, we hypothesize that the positive abrupt change in single-year shape change in 2017 may be related to the subsidence of the subsurface due to groundwater and rivers. Changes in groundwater due to extreme precipitation cause the regional subsurface to bulge [86], leading to a single-year bulge in the monitored deformation results, while heavy precipitation will cause a significant increase in river sand transport, leading to significant erosion along the banks of the river.

The multi-year deformation analysis showed that the central plain and hilly area had obvious subsidence. The general terrain of Yanshou County slopes from south toward north in the middle, and from southwest to northeast in the middle, where plains and hills are distributed in the central and peripheral areas, and the valley bottom is an alluvial plain among the mountains, most of the plain being cultivated. Sloping cultivated land is the main source of soil and water loss in the BSR, which is closely related to the thinning of the black soil layer [87]. Compared with the anomalous uplift monitored in the single-year results, the five-year deformation trend was basically consistent with the current erosion status of the black soil zone. Wang et al. [88] reported an erosion rate of the black soil zone of −2.22 mm yr^{-1}, based on a $^{137}C_S$ tracer study of 12 black soil profiles. A total erosion of −11 mm over a 5-year period was reported in the BSR, with Yanshou County situated within its sub-region. Notably, our multi-year deformation monitoring using D-InSAR yielded a similar trend, with a mean value of −11.1 mm. This indicates that the use of

InSAR technology to investigate the current situation of long-term soil erosion in the black soil zone has great potential.

4.2. Mechanisms and Drivers of Regional Deformation Rate Changes

The average value of deformation rate of the time nodes was negative for the whole of 2017, except for January and February, showing the state of overall subsidence of the region. With increasing time, the cumulative deformation rate continued to increase in the negative direction, and the phenomenon of subsidence became increasingly significant. Cumulative deformation rate counting by time nodes and the relationship between temperature, precipitation, snow thickness, and other related variables showed that the BSR in Yanshou County may be affected by multi-camp force composite erosion. Freeze–thaw erosion is a phenomenon in which the water in the soil expands when it freezes, leading to an increase in the number of fissures, the fragmentation of the whole soil body, a decrease in the erosion resistance stability after ablation, and deformation and displacement under the action of gravity, which usually occur in the spring, when the snow and the ice melt [89]. The SBAS-InSAR results showed that, as the temperature increased in the spring (March), the snow accumulated during the winter melted in the spring to form snowmelt runoff, and the cumulative deformation rate of the sub-nodes changed significantly from 3.279 to -2.805 mm yr^{-1}, which indicated that the soil erosion in the region was intensifying. The wavelet analysis of the deformation rate and temperature revealed that when the temperature increases at the onset of spring, the change in surface rate is closely correlated to the surface temperature (relevance > 0.9). By comparison, the erosion rate area flattens out in the winter season (after September) with the gradual decrease in temperature (Figure 10a). Therefore, the deformation of the BSR in Yanshou County appears to be closely related to the freezing and thawing erosion [60,90–92].

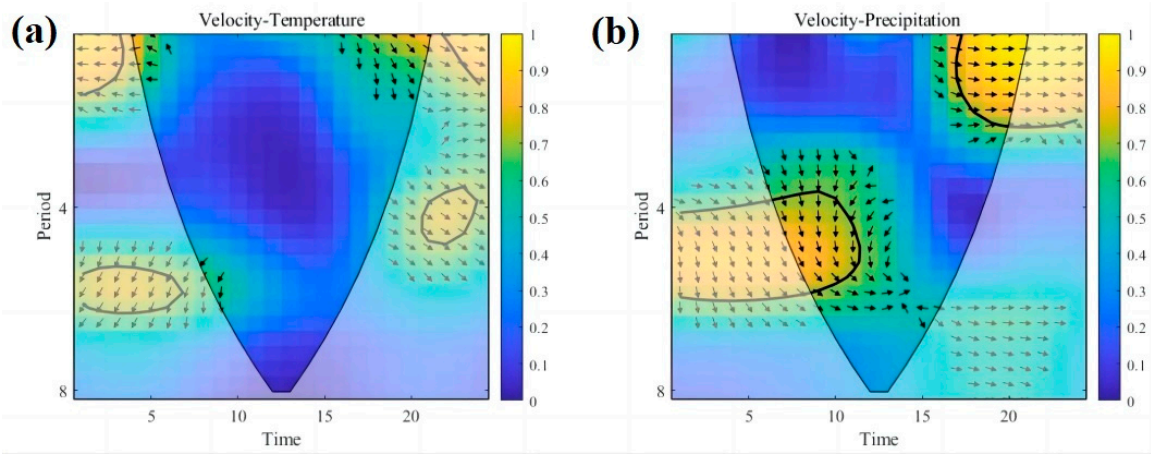

Figure 10. Wavelet analysis [93] between velocity and temperature (**a**) and precipitation (**b**) The arrows denote the relative phase relationship (in-phase, arrows point right; anti-phase, arrows point left), and the color denotes the strength of coherence.

The deformation rate decreased with increasing precipitation in April. At the end of August, with the peak of precipitation, the sedimentation rate also reached the quarterly peak, from ~-3 to ~-6 mm yr^{-1}. With the end of precipitation on 8 December, the sedimentation rate reached a peak of -7.318 mm yr^{-1}, which revealed that the deformation of the BSR was closely related to precipitation. The effect of precipitation on regional erosion and sedimentation was longer lasting than the effect of temperature on deformation rate and showed an obvious correlation between summer and winter, with erosion velocity increasing negatively with increasing precipitation intensity. Meanwhile, the effect of precipitation (snowfall) on erosion velocity was smoother and more weakly correlated in winter than in summer (Figure 10b). The increase in water content is a significant contributing factor that diminishes surface friction between stacked materials, leading to

additional surface deformation [89]. Moreover, the observed rate of deformation exhibits a weak correlation with soil water content, indicating the relative importance of these features, potentially influenced by data resolution. The deformation of the region cannot fully represent the current erosion status. However, it partially reflected the trend of regional erosion. Our findings indicate a strong correlation between regional deformation and freeze–thaw cycles, as well as precipitation factors. The BSR of Yanshou County was therefore subjected to the composite effect of freeze–thaw erosion [94,95] and precipitation erosion.

Constraints remain in the study of deformation drivers in Yanshou County. The types of erosion in the northeastern black soil zone mainly included hydraulic erosion, wind erosion, freeze–thaw erosion, and gravity erosion. Due to the limitations of data resolution, it was difficult to quantify the effect of wind erosion on the deformation of the black soil zone. The surface deformation can also be associated with natural disasters, such as landslides and avalanches. However, both landslides and avalanches can be considered as displacements of soil under external stresses, resulting in changes in the thickness of the soil layer. Therefore, they can be regarded as erosion phenomena caused by the intense scouring of the soil body. There are few published studies related to gravity erosion, the mechanism of which is still unclear, so we were unable to find the relevant variables needed to explore in-depth the effect of gravity erosion on the deformation of the region.

4.3. Implications of Erosion Susceptibility Analyses for Regional Black Soil Conservation

There is a significant risk of erosion in the region, with more than 70% of the area being susceptible to soil erosion. The region is subjected to the compound influence of hydraulic erosion and freeze–thaw erosion, leading to severe scouring during the summer months, which poses threats to agricultural production and human safety. The erosion susceptibility analysis revealed that altitude and slope exert a substantial influence on erosion within the area. Erosion gradually weakens from high-altitude areas to low-altitude regions, consistent with previous research findings that emphasize the need for regular monitoring in the high-altitude hilly areas of Yanshou County to prevent disasters. However, some high-elevation locations exhibit an opposite trend, where soil deposition occurs, potentially due to interactions between elevation, slope, vegetation cover, and other factors. Adequate vegetation cover plays a crucial role in reducing erosion risk within the region while also contributing towards wind prevention and soil stabilization, albeit to a limited extent.

The susceptibility analysis revealed that the region is prone to gully erosion and scouring, which may be attributed to monocropping practices. In Yanshou County, although the vegetation cover is relatively high at 69.2%, conventional perceptions would not anticipate severe soil erosion. However, it should be noted that barren mountains and wastelands account for 11.5% of the total area, which is predominantly characterized by swampy pastures as the main vegetation type. Additionally, extensive farmland and sloping arable land within the region are subjected to more severe gully erosion due to the topographic structure and multiple river basins [96]. To mitigate the cropland erosion caused by cultivation practices, it is recommended to prioritize straw incorporation and integrate crop rotation, deep plowing, reduced tillage or no-tillage methods with erosion-prevention measures. For large areas of sloping arable land, protective plowing should be adopted, along with improved farmland runoff drainage measures and the management of erosion gullies on farmland and roads. Additionally, contour plowing and horizontal terraces can be established to reduce soil erosion on sloping arable land. Additionally, effective planting structures, along with on-farm water storage and irrigation facilities, are imperative to mitigate diffuse, irrigation-induced secondary soil erosion.

The erosion susceptibility analysis demonstrated the potential for sedimentation on both riverbanks, with the sediment subsequently migrating to adjacent areas due to summer river scouring effects. To safeguard these riparian zones, it is recommended to implement an integrated management strategy for small watersheds, aimed at preserving vegetation on both sides of the river. Furthermore, in specific regions, consideration should be given to

constructing ditch storage projects and implementing flash flood and debris flow drainage systems as measures to mitigate watershed damage during the flood season.

4.4. Shortcomings and Prospects of Using InSAR Technology to Monitor Soil Erosion in the BSR

Although the use of InSAR technology for monitoring soil erosion changes in the black soil area (BSR) meets large-scale monitoring requirements and ensures high accuracy, it has several limitations. These include the following: (1) the susceptibility of InSAR technology to errors caused by vegetation and topography, particularly in areas with dense vegetation cover and gullies; (2) the number of training samples for machine learning is limited to 10% of the total due to restrictions on the GEE platform; and (3) for multi-year erosion research, it is essential to consider that deformation may result from variations in the water table or crustal movement, and not solely from erosion. Therefore, the impact of multiple factors on monitoring results must be considered.

To address the limitations of InSAR in monitoring soil erosion, future studies should consider the following measures to mitigate errors caused by multiple factors, so as to further enhance the accuracy of regional erosion monitoring: (1) utilizing measured data or Unmanned Aerial Vehicle (UAV) data to reconstruct the regional deformation and rectify InSAR inaccuracies [97,98]; (2) quantifying the changes in regional groundwater and settlement of built-up areas by employing Gravity Recovery and Climate Experiment (GRACE) data and building information mode (BIM) technology, for example, to eliminate the influence of groundwater table fluctuations and earth movement; and (3) conducting research on a large watershed scale with comprehensive monitoring data on river discharge and sediment yield.

5. Conclusions

The black soil region in Northeast China currently faces challenges such as thinning, compaction, and degradation. This study aimed to efficiently and accurately capture and analyze the spatial and temporal distribution characteristics of soil erosion at medium and large scales. The ultimate goal was to comprehensively map the current state of erosion in Northeast China's BSR, providing essential data and scientific references for effective conservation measures and the sustainable development of this valuable resource. In this study, we employed diverse InSAR techniques to monitor and assess the regional deformation variables and rates in Yanshou County, Heilongjiang Province. Furthermore, machine learning algorithms were applied to analyze the susceptibility to erosion based on the obtained rates as training samples. The proposed InSAR-based regional-scale black soil erosion monitoring technique provides an effective means of investigating and assessing black soil erosion. Despite the influence of external factors such as vegetation, groundwater, and crustal movement on current InSAR techniques, the results closely align with measured data, demonstrating their practical significance. The region was subject to the compound influence of hydraulic and freeze–thaw erosion, which was closely related to crop phenology. The susceptibility analysis indicated that good vegetation cover reduces the risk of soil erosion to a certain extent. Therefore, the application of machine learning in erosion susceptibility analysis offers a valuable framework for developing soil and water conservation measures in Yanshou County. Its potential extension to a broader black soil region promises to enhance the monitoring and protection of this invaluable resource. To mitigate potential loss in the river basin during the flood season, it is recommended to implement comprehensive small watershed management strategies, safeguard riparian vegetation, and construct gully water storage facilities, as well as mountain flood and debris flow drainage systems in select areas.

Supplementary Materials: The following supporting information can be downloaded at: https://www.mdpi.com/article/10.3390/rs16203842/s1, Captions: RUSLE and phenological information calculation method and erosion susceptibility analysis code Figure S1: Results of the calculation of phenological information: (a) timing of the beginning of the growing season (b) timing of the end of the growing season (c) duration of the growing season. Figure S2. The overall logic frame diagram.

Figure S3. Flowchart of D-InSAR technique to acquire surface morphology variables. Figure S4. Flowchart of SBAS-InSAR technique to acquire surface deformation rate. Figure S5. Temporal (left) and spatial (right) baseline connection graph of interferogram pairs. Figure S6. Sample data sampling distribution for sensitivity analysis. Sample data for machine learning model training with 5000 points sampled from 106,635 SBAS-InSAR cumulative deformation rate points, where black represents the spatial distribution of the sample d data.

Author Contributions: H.H. conceptualized this study; Y.G., J.Y. and H.H. wrote the original paper; H.H., J.Y., X.W., X.C., J.L., N.A. and F.Z. All authors have read and agreed to the published version of the manuscript.

Funding: This research was funded by the National Key Research and Development Program of China grant number [2022YFD1500103] and the High-End Foreign Experts Project from the Ministry of Science and Technology, China grant number [G2022172040L and G2023172014L].

Data Availability Statement: All relevant data and code are within the manuscript and its Supplementary Materials. The data that support the findings of this study are openly available at https://dataverse.harvard.edu/dataset.xhtml?persistentId=doi:10.7910/DVN/TJUKE8, accessed on 5 September 2024.

Acknowledgments: The datasets used in this study were digitalized from the published literature. Funding for this research was provided in part by the National Key Research and Development Program of China (2022YFD1500103) and the High-End Foreign Experts Project from the Ministry of Science and Technology, China (G2022172040L and G2023172014L).

Conflicts of Interest: The authors declare no conflict of interest.

References

1. Liu, J.; Sui, Y.; Yu, Z.; Shi, Y.; Chu, H.; Jin, J.; Liu, X.; Wang, G. Soil carbon content drives the biogeographical distribution of fungal communities in the black soil zone of northeast China. *Soil Biol. Biochem.* **2015**, *83*, 29–39. [CrossRef]
2. Yadav, D.; Vishwakarma, A.K.; Sharma, N.K.; Biswas, A.K.; Ojasvi, P.R.; Kumar, D.; Kumawat, A.; Singh, D. Sustaining the properties of black soil in Central India through crop residue management in a conservation-agriculture-based soybean–wheat system. *Land Degrad. Dev.* **2021**, *32*, 2906–2921. [CrossRef]
3. Liu, X.; Burras, C.L.; Kravchenko, Y.S.; Duran, A.; Huffman, T.; Morras, H.; Studdert, G.; Zhang, X.; Cruse, R.M.; Yuan, X. Overview of Mollisols in the world: Distribution, land use and management. *Can. J. Soil Sci.* **2012**, *92*, 383–402. [CrossRef]
4. Hu, X.; Liu, J.; Zhu, P.; Wei, D.; Jin, J.; Liu, X.; Wang, G. Long-term manure addition reduces diversity and changes community structure of diazotrophs in a neutral black soil of northeast China. *J. Soils Sediments* **2018**, *18*, 2053–2062. [CrossRef]
5. Wang, B.; Hao, J.; Meng, D.; Li, W.; Yuan, Q. Methods of land consolidation in chernozems region of China. *Trans. Chin. Soc. Agric. Eng. (Trans. CSAE)* **2008**, *24*, 44–48.
6. Zhu, G.; Tang, Z.; Shangguan, Z.; Peng, C.; Deng, L. Factors affecting the spatial and temporal variations in soil erodibility of China. *J. Geophys. Res. Earth Surf.* **2019**, *124*, 737–749. [CrossRef]
7. FAO. *Global Status of Black Soils*; FAO: Rome, Italy, 2022.
8. Tang, J.; Liu, G.; Xie, Y.; Wu, Y.; Wang, D.; Gao, Y.; Meng, L. Effect of topographic variations and tillage methods on gully erosion in the black soil region: A case-study from Northeast China. *Land Degrad. Dev.* **2022**, *33*, 3786–3800. [CrossRef]
9. An, J.; Zheng, F.; Wang, B. Using 137Cs technique to investigate the spatial distribution of erosion and deposition regimes for a small catchment in the black soil region, Northeast China. *CATENA* **2014**, *123*, 243–251. [CrossRef]
10. Fang, H. Impacts of land use and soil conservation measures on runoff and soil loss from two contrasted soils in the black soil region, northeastern China. *Hydrol. Process.* **2023**, *37*, e14886. [CrossRef]
11. Saez, J.L.; Corona, C.; Stoffel, M.; Rovéra, G.; Astrade, L.; Berger, F. Mapping of erosion rates in marly badlands based on a coupling of anatomical changes in exposed roots with slope maps derived from LiDAR data. *Earth Surf. Process. Landf.* **2011**, *36*, 1162–1171. [CrossRef]
12. Li, P.; Hao, M.; Hu, J.; Gao, C.; Zhao, G.; Chan, F.K.S.; Gao, J.; Dang, T.; Mu, X. Spatiotemporal Patterns of Hillslope Erosion Investigated Based on Field Scouring Experiments and Terrestrial Laser Scanning. *Remote Sens.* **2021**, *13*, 1674. [CrossRef]
13. Imamoglu, A.; Dengiz, O. Determination of soil erosion risk using RUSLE model and soil organic carbon loss in Alaca catchment (Central Black Sea region, Turkey). *Rend. Fis. Acc. Lincei* **2016**, *28*, 11–23. [CrossRef]
14. Wang, R.; Zhang, S.; Yang, J.; Pu, L.; Yang, C.; Yu, L.; Chang, L.; Bu, K. Integrated Use of GCM, RS, and GIS for the Assessment of Hillslope and Gully Erosion in the Mushi River Sub-Catchment, Northeast China. *Sustainability* **2016**, *8*, 317. [CrossRef]
15. Yang, X.M.; Zhang, X.P.; Deng, W.; Fang, H.J. Black soil degradation by rainfall erosion in Jilin, China. *Land Degrad. Dev.* **2003**, *14*, 409–420. [CrossRef]
16. Diodato, N.; Borrelli, P.; Fiener, P.; Bellocchi, G.; Romano, N. Discovering historical rainfall erosivity with a parsimonious approach: A case study in Western Germany. *J. Hydrol.* **2017**, *544*, 1–9. [CrossRef]

17. Douglas-Mankin, K.R.; Srinivasan, R.; Arnold, J.G. Soil and Water Assessment Tool (SWAT) model: Current developments and applications. *Trans. ASABE* **2010**, *53*, 1423–1431. [CrossRef]
18. Krysanova, V.; Müller-Wohlfeil, D.-I.; Becker, A. Development and test of a spatially distributed hydrological/water quality model for mesoscale watersheds. *Ecol. Model.* **1998**, *106*, 261–289. [CrossRef]
19. Gassman, P.W.; Williams, J.R.; Wang, X.; Saleh, A.; Osei, E.; Hauck, L.M.; Izaurralde, R.C.; Flowers, J.D. Invited Review Article: The Agricultural Policy/Environmental eXtender (APEX) Model: An Emerging Tool for Landscape and Watershed Environmental Analyses. *Trans. ASABE* **2010**, *53*, 711–740. [CrossRef]
20. Williams, J.R.; Arnold, J.G.; Kiniry, J.R.; Gassman, P.W.; Green, C.H. History of model development at Temple, Texas. *Hydrol. Sci. J.* **2008**, *53*, 948–960. [CrossRef]
21. Fang, H. Impact of Land Use Change and Dam Construction on Soil Erosion and Sediment Yield in the Black Soil Region, Northeastern China. *Land Degrad. Dev.* **2017**, *28*, 1482–1492. [CrossRef]
22. Lieskovský, J.; Kenderessy, P. Modelling the effect of vegetation cover and different tillage practices on soil erosion in vineyards: A case study in Vráble (Slovakia) using WATEM/SEDEM. *Land Degrad. Dev.* **2014**, *25*, 288–296. [CrossRef]
23. DeRoo, A.P.J.; Wesseling, C.G.; Ritsema, C.J. LISEM: A single-event physically based hydrological and soil erosion model for drainage basins. I: Theory, input and output. *Hydrol. Process.* **1996**, *10*, 1107–1117. [CrossRef]
24. Jetten, V.; Govers, G.; Hessel, R. Erosion models: Quality of spatial predictions. *Hydrol. Process.* **2003**, *17*, 887–900. [CrossRef]
25. Li, X.R.; Wang, X.P.; Li, T.; Zhang, J.G. Microbiotic soil crust and its effect on vegetation and habitat on artificially stabilized desert dunes in Tengger Desert, North China. *Biol. Fertil. Soils* **2002**, *35*, 147–154. [CrossRef]
26. Fernández, C.; Vega, J.A.; Vieira, D. Assessing soil erosion after fire and rehabilitation treatments in NW Spain: Performance of rusle and revised Morgan-Morgan-Finney models. *Land Degrad. Dev.* **2010**, *21*, 58–67. [CrossRef]
27. Mondal, A.; Khare, D.; Kundu, S. A comparative study of soil erosion modelling by MMF, USLE and RUSLE. *Geocarto Int.* **2018**, *33*, 89–103. [CrossRef]
28. Wei, J.-B.; Xiao, D.-N.; Zhang, X.-Y.; Li, X.-Y. Topography and land use effects on the spatial variation of soil organic carbon: A case study in a typical small watershed of the black soil region in northeast China. *Eurasian Soil Sci.* **2018**, *41*, 39–47. [CrossRef]
29. Sankey, J.B.; Sankey, T.T.; Li, J.; Ravi, S.; Wang, G.; Caster, J.; Kasprak, A. Quantifying plant-soil-nutrient dynamics in rangelands: Fusion of UAV hyperspectral-LiDAR, UAV multispectral-photogrammetry, and ground-based LiDAR-digital photography in a shrub-encroached desert grassland. *Remote Sens. Environ.* **2020**, *253*, 112223. [CrossRef]
30. Wang, R.; Zhang, S.; Pu, L.; Yang, J.; Yang, C.; Chen, J.; Guan, C.; Wang, Q.; Chen, D.; Fu, B.; et al. Gully Erosion Mapping and Monitoring at Multiple Scales Based on Multi-Source Remote Sensing Data of the Sancha River Catchment, Northeast China. *ISPRS Int. J. Geo-Inf.* **2016**, *5*, 200. [CrossRef]
31. Barbiéro, L.; Parate, H.R.; Descloitres, M.; Bost, A.; Furian, S.; Kumar, M.M.; Kumar, C.; Braun, J.-J. Using a structural approach to identify relationships between soil and erosion in a semi-humid forested area, South India. *CATENA* **2007**, *70*, 313–329. [CrossRef]
32. Dai, T.; Wang, L.; Li, T.; Qiu, P.; Wang, J. Study on the Characteristics of Soil Erosion in the Black Soil Area of Northeast China under Natural Rainfall Conditions: The Case of Sunjiagou Small Watershed. *Sustainability* **2022**, *14*, 8284. [CrossRef]
33. Wang, R.; Sun, H.; Yang, J.; Zhang, S.; Fu, H.; Wang, N.; Liu, Q. Quantitative Evaluation of Gully Erosion Using Multitemporal UAV Data in the Southern Black Soil Region of Northeast China: A Case Study. *Remote Sens.* **2022**, *14*, 1479. [CrossRef]
34. Alexandridis, T.K.; Monachou, S.; Skoulikaris, C.; Kalopesa, E.; Zalidis, G.C. Investigation of the temporal relation of remotely sensed coastal water quality with GIS modelled upstream soil erosion. *Hydrol. Process.* **2014**, *29*, 2373–2384. [CrossRef]
35. Wang, Q.; Guo, P.; Dong, S.; Liu, Y.; Pan, Y.; Li, C. Extraction of Cropland Spatial Distribution Information Using Multi-Seasonal Fractal Features: A Case Study of Black Soil in Lishu County, China. *Agriculture* **2023**, *13*, 486. [CrossRef]
36. Ferretti, A.; Prati, C.; Rocca, F. Nonlinear subsidence rate estimation using permanent scatterers in differential SAR interferometry. *IEEE Trans. Geosci. Remote Sens.* **2000**, *38*, 2202–2212. [CrossRef]
37. Rodriguez, E.; Martin, J. Theory and design of interferometric synthetic aperture radars. *IEE Proc. F Radar Signal Process.* **1992**, *139*, 147–159. [CrossRef]
38. Ferretti, A.; Prati, C.; Rocca, F. Permanent scatterers in SAR interferometry. *IEEE Trans. Geosci. Remote Sens.* **2001**, *39*, 8–20. [CrossRef]
39. Metternicht, G.; Hurni, L.; Gogu, R. Remote sensing of landslides: An analysis of the potential contribution to geo-spatial systems for hazard assessment in mountainous environments. *Remote Sens. Environ.* **2005**, *98*, 284–303. [CrossRef]
40. Tralli, D.M.; Blom, R.G.; Zlotnicki, V.; Donnellan, A.; Evans, D.L. Satellite remote sensing of earthquake, volcano, flood, landslide and coastal inundation hazards. *ISPRS J. Photogramm. Remote Sens.* **2005**, *59*, 185–198. [CrossRef]
41. Rajaneesh, A.; Logesh, N.; Vishnu, C.L.; Bouali, E.H.; Oommen, T.; Midhuna, V.; Sajinkumar, K.S. Monitoring and Mapping of Shallow Landslides in a Tropical Environment Using Persistent Scatterer Interferometry: A Case Study from the Western Ghats, India. *Geomatics* **2020**, *1*, 3–17. [CrossRef]
42. Erban, L.E.; Gorelick, S.M.; Zebker, H.A. Groundwater extraction, land subsidence, and sea-level rise in the Mekong Delta, Vietnam. *Environ. Res. Lett.* **2014**, *9*, 084010. [CrossRef]
43. Hoffmann, J.; Zebker, H.A.; Galloway, D.L.; Amelung, F. Seasonal subsidence and rebound in Las Vegas Valley, Nevada, observed by synthetic aperture radar interferometry. *Water Resour. Res.* **2001**, *37*, 1551–1566. [CrossRef]

44. Fan, X.; Xu, Q.; Alonso-Rodriguez, A.; Subramanian, S.S.; Li, W.; Zheng, G.; Dong, X.; Huang, R. Successive landsliding and damming of the Jinsha River in eastern Tibet, China: Prime investigation, early warning, and emergency response. *Landslides* **2019**, *16*, 1003–1020. [CrossRef]
45. Qu, F.; Zhang, Q.; Lu, Z.; Zhao, C.; Yang, C.; Zhang, J. Land subsidence and ground fissures in Xi'an, China 2005–2012 revealed by multi-band InSAR time-series analysis. *Remote Sens. Environ.* **2014**, *155*, 366–376. [CrossRef]
46. Jonsson, S.; Zebker, H.; Segall, P.; Amelung, F. Fault slip distribution of the 1999 M-w 7.1 Hector Mine, California, earthquake, estimated from satellite radar and GPS measurements. *Bull. Seismol. Soc. Am.* **2002**, *92*, 1377–1389. [CrossRef]
47. Xu, C.; Liu, Y.; Wen, Y.; Wang, R. Coseismic Slip Distribution of the 2008 Mw 7.9 Wenchuan Earthquake from Joint Inversion of GPS and InSAR Data. *Bull. Seism. Soc. Am.* **2010**, *100*, 2736–2749. [CrossRef]
48. Zhao, C.; Lu, Z.; Zhang, Q.; de la Fuente, J. Large-area landslide detection and monitoring with ALOS/PALSAR imagery data over Northern California and Southern Oregon, USA. *Remote Sens. Environ.* **2012**, *124*, 348–359. [CrossRef]
49. Du, Z.; Gao, B.; Ou, C.; Du, Z.; Yang, J.; Batsaikhan, B.; Dorjgotov, B.; Yun, W.; Zhu, D. A Quantitative Analysis of Factors Influencing Organic Matter Concentration in the Topsoil of Black Soil in Northeast China Based on Spatial Heterogeneous Patterns. *ISPRS Int. J. Geo-Inf.* **2021**, *10*, 348. [CrossRef]
50. Xiong, Z.; Feng, G.; He, L.; Wang, H.; Wei, J. Reactivation/Acceleration of Landslides Caused by the 2018 Baige Landslide-Dammed Lake and its Breach Floods Revealed by InSAR and Optical Images. *IEEE J. Sel. Top. Appl. Earth Obs. Remote Sens.* **2024**, *17*, 1656–1672. [CrossRef]
51. Pooja, B.; Oommen, T.; Sajinkumar, K.S.; Nair, A.G.; Rajaneesh, A.; Aswathi, J.; Bouali, E.H.; Thrivikramji, K.P. Correspondence of PSInSAR monitoring and Settle3 modelling at Cochin International Airport, SW India. *Appl. Geomat.* **2021**, *13*, 735–746. [CrossRef]
52. Sun, Q.; Jiang, L.; Jiang, M.; Lin, H.; Ma, P.; Wang, H. Monitoring Coastal Reclamation Subsidence in Hong Kong with Distributed Scatterer Interferometry. *Remote Sens.* **2018**, *10*, 1738. [CrossRef]
53. Gong, W.; Darrow, M.M.; Meyer, F.J.; Daanen, R.P. Reconstructing movement history of frozen debris lobes in northern Alaska using satellite radar interferometry. *Remote Sens. Environ.* **2018**, *221*, 722–740. [CrossRef]
54. Lei, Y.; Treuhaft, R.; Keller, M.; Dos-Santos, M.; Gonçalves, F.; Neumann, M. Quantification of selective logging in tropical forest with spaceborne SAR interferometry. *Remote Sens. Environ.* **2018**, *211*, 167–183. [CrossRef]
55. Aswathi, J.; Sajinkumar, K.S.; Rajaneesh, A.; Oommen, T.; Bouali, E.H.; Binoj Kumar, R.B.; Rani, V.R.; Thomas, J.; Thrivikramji, K.P.; Ajin, R.S.; et al. Furthering the precision of RUSLE soil erosion with PSInSAR data: An innovative model. *Geocarto International* **2022**, *37*, 16108–16131. [CrossRef]
56. Tong, Y.; Zhijie, Z.; Xiaoke, W. Feasibility Study on Monitoring Soil Erosion Using Persistent Scatterer Synthetic Aperture Radar Interferometry Technology. *Trans. Chinese Soc. Agric. Eng. (Trans. CSAE)* **2021**, *37*, 127–134.
57. Dong, Y.; Wu, Y.; Qin, W.; Guo, Q.; Yin, Z.; Duan, X. The gully erosion rates in the black soil region of northeastern China: Induced by different processes and indicated by different indexes. *CATENA* **2019**, *182*, 104146. [CrossRef]
58. Chinese Academy of Sciences. The Black Soil Conservation and Utilization Report. 2021. Available online: https://www.cas.cn/zt/kjzt/htlc/yxdt/202210/W020221002625709353750.pdf (accessed on 5 September 2024).
59. Wang, H.; Yang, S.; Wang, Y.; Gu, Z.; Xiong, S.; Huang, X.; Sun, M.; Zhang, S.; Guo, L.; Cui, J.; et al. Rates and causes of black soil erosion in Northeast China. *CATENA* **2022**, *214*, 106250. [CrossRef]
60. Zhai, Y.; Fang, H. Spatiotemporal variations of freeze-thaw erosion risk during 1991–2020 in the black soil region, northeastern China. *Ecol. Indic.* **2023**, *148*, 110149. [CrossRef]
61. Wang, Z.; Liu, B.; Wang, X.; Gao, X.; Liu, G. Erosion effect on the productivity of black soil in Northeast China. *Sci. China Ser. D Earth Sci.* **2009**, *52*, 1005–1021. [CrossRef]
62. Zhao, P.; Li, S.; Wang, E.; Chen, X.; Deng, J.; Zhao, Y. Tillage erosion and its effect on spatial variations of soil organic carbon in the black soil region of China. *Soil Tillage Res.* **2018**, *178*, 72–81. [CrossRef]
63. Torres, R.; Snoeij, P.; Geudtner, D.; Bibby, D.; Davidson, M.; Attema, E.; Potin, P.; Rommen, B.; Floury, N.; Brown, M.; et al. GMES Sentinel-1 mission. *Remote Sens. Environ.* **2012**, *120*, 9–24. [CrossRef]
64. Yu, C.; Penna, N.T.; Li, Z. Generation of real-time mode high-resolution water vapor fields from GPS observations. *J. Geophys. Res. Atmos.* **2017**, *122*, 2008–2025. [CrossRef]
65. Yu, C.; Li, Z.; Penna, N.T.; Crippa, P. Generic atmospheric correction model for interferometric synthetic aperture radar observations. *J. Geophys. Res. Solid Earth* **2018**, *123*, 9202–9222. [CrossRef]
66. Chatterjee, R.; Fruneau, B.; Rudant, J.; Roy, P.; Frison, P.-L.; Lakhera, R.; Dadhwal, V.; Saha, R. Subsidence of Kolkata (Calcutta) City, India during the 1990s as observed from space by Differential Synthetic Aperture Radar Interferometry (D-InSAR) technique. *Remote Sens. Environ.* **2006**, *102*, 176–185. [CrossRef]
67. Lee, C.W.; Lu, Z.; Jung, H.S.; Won, J.S.; Dzurisin, D. Surface Deformation of Augustine Volcano, 1992–2005, from Multiple-Interferogram Processing Using a Refined Small Baseline Subset (SBAS) Interferometric Synthetic Aperture Radar (InSAR) Approach. *The* **2006**, *2*, 453–465.
68. Li, X.; Zhou, Y.; Asrar, G.R.; Meng, L. Characterizing spatiotemporal dynamics in phenology of urban ecosystems based on Landsat data. *Sci. Total. Environ.* **2017**, *605–606*, 721–734. [CrossRef]
69. Patil, P.M.; Shashikant, A.; Roy, S.; Momoniat, E. Unsteady Mixed Convection over an Exponentially Decreasing External Flow Velocity. *Int. J. Heat Mass Transfer* **2017**, *111*, 643–650. [CrossRef]

70. Williams, J.; Sharpley, A.; Taylor, D. Assessing the Impact of Erosion on Soil Productivity Using the EPIC Model. In *Soil Erosion on Agricultural Land*; Williams, J., Sharpley, A., Taylor, D., Eds.; John Wiley & Sons Ltd.: Coventry, UK, 1990; pp. 461–464. Available online: https://www.jstor.org/stable/76847 (accessed on 5 September 2024).
71. Moore, I.D.; Wilson, J.P. Length-Slope Factors for the Revised Universal Soil Loss Equation: Simplified Method of Estimation. *J. Soil Water Conserv.* **1992**, *47*, 423–428.
72. Van der Knijff, J.M.; Jones, R.J.A.; Montanarella, L. Soil Erosion Risk Assessment in Europe. 2000. Available online: https://www.researchgate.net/publication/237727657_Soil_Erosion_Risk_Assessment_in_Europe (accessed on 5 September 2024).
73. Gelagay, H.S.; Minale, A.S. Soil Loss Estimation Using GIS and Remote Sensing Techniques: A Case of Koga Watershed, Northwestern Ethiopia. *Int. Soil Water Conserv. Res.* **2016**, *4*, 126–136. [CrossRef]
74. Fisher, J.I.; Mustard, J.F.; Vadeboncoeur, M.A. Green leaf phenology at Landsat resolution: Scaling from the field to the satellite. *Remote Sens. Environ.* **2006**, *100*, 265–279. [CrossRef]
75. Zhu, W.; He, B.; Xie, Z.; Zhao, C.; Zhuang, H.; Li, P. Reconstruction of Vegetation Index Time Series Based on Self-Weighting Function Fitting from Curve Features. *Remote Sens.* **2022**, *14*, 2247. [CrossRef]
76. Beck, P.S.; Atzberger, C.; Høgda, K.A.; Johansen, B.; Skidmore, A.K. Improved monitoring of vegetation dynamics at very high latitudes: A new method using MODIS NDVI. *Remote. Sens. Environ.* **2006**, *100*, 321–334. [CrossRef]
77. Yu, C.; Li, Z.; Penna, N.T. Interferometric synthetic aperture radar atmospheric correction using a GPS-based iterative tropospheric decomposition model. *Remote Sens. Environ.* **2018**, *204*, 109–121. [CrossRef]
78. Gorelick, N.; Hancher, M.; Dixon, M.; Ilyushchenko, S.; Thau, D.; Moore, R. Google Earth Engine: Planetary-scale geospatial analysis for everyone. *Remote Sens. Environ.* **2017**, *202*, 18–27. [CrossRef]
79. Huntington, J.L.; Hegewisch, K.C.; Daudert, B.; Morton, C.G.; Abatzoglou, J.T.; McEvoy, D.J.; Erickson, T. Climate Engine: Cloud Computing and Visualization of Climate and Remote Sensing Data for Advanced Natural Resource Monitoring and Process Understanding. *Bull. Am. Meteorol. Soc.* **2017**, *98*, 2397–2410. [CrossRef]
80. DeVries, B.; Huang, C.; Armston, J.; Huang, W.; Jones, J.W.; Lang, M.W. Rapid and robust monitoring of flood events using Sentinel-1 and Landsat data on the Google Earth Engine. *Remote Sens. Environ.* **2020**, *240*, 111664. [CrossRef]
81. Souza, C.M., Jr.; Shimbo, J.Z.; Rosa, M.R.; Parente, L.L.; Alencar, A.A.; Rudorff, B.F.T.; Hasenack, H.; Matsumoto, M.; Ferreira, L.G.; Souza-Filho, P.W.M.; et al. Reconstructing Three Decades of Land Use and Land Cover Changes in Brazilian Biomes with Landsat Archive and Earth Engine. *Remote Sens.* **2020**, *12*, 1735.
82. Yang, J.; Huang, X. The 30 m annual land cover dataset and its dynamics in China from 1990 to 2019. *Earth Syst. Sci. Data* **2021**, *13*, 3907–3925. [CrossRef]
83. Darvishi, M.; Destouni, G.; Aminjafari, S.; Jaramillo, F. Multi-Sensor InSAR Assessment of Ground Deformations around Lake Mead and Its Relation to Water Level Changes. *Remote. Sens.* **2021**, *13*, 406. [CrossRef]
84. Beijing Evening News, Heavy Rains Hit Northeast China's Heilongjiang and Jilin Provinces. 2017. Available online: http://epaper.pdsxww.com/pdswb/page/41/2017-07/22/A06/20170722A06_pdf.pdf (accessed on 5 September 2024).
85. Zhang, S.; Zhang, Y.; Yu, J.; Fan, Q.; Si, J.; Zhu, W.; Song, M. Interpretation of the Spatiotemporal Evolution Characteristics of Land Deformation in Beijing during 2003–2020 Using Sentinel, ENVISAT, and Landsat Data. *Remote Sens.* **2022**, *14*, 2242. [CrossRef]
86. Jan, C.-D.; Chen, T.-H.; Lo, W.-C. Effect of rainfall intensity and distribution on groundwater level fluctuations. *J. Hydrol.* **2006**, *332*, 348–360. [CrossRef]
87. Zhang, M.; Zhang, W.; Zhang, K.; Yu, Y.; Liu, L. Centennial scale temporal responses of soil magnetic susceptibility and spatial variation to human cultivation on hillslopes in Northeast China. *Soil Tillage Res.* **2023**, *234*, 105865. [CrossRef]
88. Wang, S.; Cui, G.; Li, X.; Liu, Y.; Li, X.; Tong, S.; Zhang, M. GRACE Satellite-Based Analysis of Spatiotemporal Evolution and Driving Factors of Groundwater Storage in the Black Soil Region of Northeast China. *Remote Sens.* **2023**, *15*, 704. [CrossRef]
89. Yan, Y.; Yu, H.; Wang, Y. Alarming a tailings dam failure with a joint analysis of InSAR-derived surface deformation and SAR-derived moisture content. *Remote Sens. Environ.* **2024**, *300*, 113910. [CrossRef]
90. Sun, B.; Ren, F.; Ding, W.; Zhang, G.; Huang, J.; Li, J.; Zhang, L. Effects of freeze-thaw on soil properties and water erosion. *Soil Water Res.* **2021**, *16*, 205–216. [CrossRef]
91. Zhao, Y.; Wang, E.; Cruse, R.M.; Chen, X. Characterization of seasonal freeze-thaw and potential impacts on soil erosion in northeast China. *Can. J. Soil Sci.* **2012**, *92*, 567–571. [CrossRef]
92. Zhang, Y.; Li, Y.; Chen, J.; Shahir, S.; Safavi-Naeini, S. Sparse Millimeter-Wave InSAR Imaging Approach Based on MC. *IEEE Geosci. Remote Sens. Lett.* **2018**, *15*, 714–718. [CrossRef]
93. Jin, F.; Yang, W.; Fu, J.; Li, Z. Effects of vegetation and climate on the changes of soil erosion in the Loess Plateau of China. *Sci. Total Environ.* **2021**, *773*, 145514. [CrossRef]
94. Fan, H.; Liu, Y.; Xu, X.; Wu, M.; Zhou, L. Simulation of rill erosion in black soil and albic soil during the snowmelt period. *Acta Agric. Scand. Sect. B—Soil Plant Sci.* **2017**, *67*, 510–517. [CrossRef]
95. Hu, G.; Wu, Y.; Liu, B.; Yu, Z.; You, Z.; Zhang, Y. Short-term Gully Retreat Rates over Rolling Hill Areas in Black Soil of Northeast China. *Catena* **2007**, *71*, 321–329. [CrossRef]
96. Xie, Y.; Tang, J.; Gao, Y.; Gu, Z.J.; Liu, G.; Ren, X.Y. Spatial Distribution of Soil Erosion and Its Impacts on Soil Productivity in Songnen Typical Black Soil Region. *Int. Soil Water Conserv. Res.* **2023**, *11*, 649–659.

97. Yao, J.; Yao, X.; Liu, X. Landslide Detection and Mapping Based on SBAS-InSAR and PS-InSAR: A Case Study in Gongjue County, Tibet, China. *Remote Sens.* **2022**, *14*, 4728. [CrossRef]
98. Zhang, L.; Zhang, R.; Dou, J.; Hou, S.; Xiang, Z.; Wang, H.; Yang, P.; Liu, X. Advancing Reservoir Landslide Stability Assessment via TS-InSAR and Airborne LiDAR Observations in the Daping Landslide Group, Three Gorges Reservoir Area, China. *Landslides* **2024**, *21*, 327–337. [CrossRef]